J. Fluid Mech. (2009), *vol.* 636, *pp.* 91–108.
doi:10.1017/S0022112009007654

Low-mode internal tide generation by topography: an experimental and numerical investigation

PAULA ECHEVERRI[1]†, M.R. FLYNN[2]‡, KRAIG B. WINTERS[3] AND THOMAS PEACOCK[4]

[1,4]Department of Mechanical Engineering, Massachusetts Institute of Technology, Cambridge, MA 02139, USA

[2]Department of Mathematics, Massachusetts Institute of Technology, Cambridge, MA 02139, USA

[3]Scripps Institution of Oceanography and Department of Mechanical and Aerospace Engineering, University of California, San Diego, La Jolla, CA 92093, USA

(Received 15 December 2008; revised 11 April 2009; accepted 13 April 2009)

We analyse the low-mode structure of internal tides generated in laboratory experiments and numerical simulations by a two-dimensional ridge in a channel of finite depth. The height of the ridge is approximately half of the channel depth and the regimes considered span sub- to supercritical topography. For small tidal excursions, of the order of 1 % of the topographic width, our results agree well with linear theory. For larger tidal excursions, up to 15 % of the topographic width, we find that the scaled mode 1 conversion rate decreases by less than 15 %, in spite of nonlinear phenomena that break down the familiar wave-beam structure and generate harmonics and inter-harmonics. Modes two and three, however, are more strongly affected. For this topographic configuration, most of the linear baroclinic energy flux is associated with the mode 1 tide, so our experiments reveal that nonlinear behaviour does not significantly affect the barotropic to baroclinic energy conversion in this regime, which is relevant to large-scale ocean ridges. This may not be the case, however, for smaller scale ridges that generate a response dominated by higher modes.

1. Introduction

Oceanic internal tides are baroclinic wave fields of tidal period generated by barotropic tidal flow past sea-floor topography. They are believed to play an important role in oceanic mixing processes (St.Laurent & Garrett 2002). As such, there is a need to accurately model internal tide generation, in order to estimate the energy transfer from barotropic to internal tides. One conclusion drawn from field studies (Rudnick *et al.* 2003), satellite observations (Egbert & Ray 2000) and numerical simulations (Simmons, Halberg & Arbic 2004) is that steep nominally two-dimensional ocean ridges contribute significantly to the internal tide budget. This is primarily because barotropic tides are forced to flow over them, rather than being able to go around, thereby generating strong disturbances of the stratification.

† Email address for correspondence: paulae@mit.edu

‡ Present address: Department of Mechanical Engineering, University of Alberta, Edmonton, AB, Canada T6G 2G8.

While a principal focus has been to obtain accurate estimates of the energy flux into internal tides (Garrett & Kunze 2007), there are other aspects of the generation process that also demand investigation. An important one is the form of the internal wave field generated, as it is not clearly understood where and how internal tide energy is ultimately dissipated (Kunze & Llewellyn Smith 2004). The prime candidates are local mixing near generation sites, wave–wave interactions in the deep ocean, scattering by sea-floor topography or mesoscale features in the ocean and reflection at continental shelves. Determining the role of each of these candidates requires that the structure, and not just the energy flux, of radiated internal tides is well captured by models.

A means of characterizing the structure of an internal tide in a finite-depth ocean is to decompose it into the vertical basis modes of the local density stratification. This technique is regularly applied to oceanographic data (Nash, Alford & Kunze 2005). Low modes (i.e. modes with a relatively large vertical length scale) have been found to propagate far away from generation sites (Ray & Mitchum 1997), and are thus able to participate in wave–wave interactions, scattering or reflection from continental shelves. In contrast, higher modes (i.e. modes with a relatively small vertical length scale) propagate more slowly, are more susceptible to instability and could contribute to local mixing near the generation site. This local mixing, however, is postulated to not significantly impact the radiation of low modes, which, in configurations where the topography is tall with respect to the ocean depth, transport a majority of the internal tide energy away from the generation site (Kunze & Llewellyn Smith 2004; Di Lorenzo, Young & Llewellyn Smith 2006).

One current analytical model of internal tide generation is a Green's function approach to solve for linear periodic wave fields generated by an arbitrarily steep topographic feature in a finite-depth ocean (Pétrélis, Llewellyn Smith & Young 2006). The approach is restricted to regimes with a linear background stratification, although a separate methodology exists for the limiting case of knife-edge topography, for which tractable solutions may be obtained for arbitrary stratifications (Llewellyn Smith & Young 2003). The far-field tidal excursion δ (half the peak-to-peak excursion) is assumed to be small such that, except for the extreme case of a knife-edge barrier, the excursion parameter

$$\chi = \frac{\delta}{a}, \tag{1.1}$$

where a is a characteristic (one-sided) horizontal length scale associated with the topography, is also small. Two additional dimensionless parameters that naturally arise are the criticality ε (i.e. ratio of the maximum topographic slope to the internal ray slope) and the depth ratio Λ/h (i.e. ratio of the maximum topographic height Λ to the ocean depth h). Estimates of the energy flux and modal structure of internal wave fields can be made based on these latter two parameters. The model predicts singular features for critical and supercritical topography, however, and it is not clear what their physical implications are.

Herein, we examine the excitation of internal tides by a Gaussian ridge with depth ratio $\Lambda/h \approx 0.5$, which is relevant to important sites of internal tide generation such as Hawaii; and focus on the generation of low modes (1–3) in a linear stratification. We investigate experimentally and numerically the radiated modal amplitudes and phases as functions of the criticality and the excursion parameters and make comparisons to the linear theory of Pétrélis *et al.* (2006), accounting for the effect of molecular viscosity in a lab-scale experiment. Beginning with a brief review of relevant theory in § 2, we move on to describe the experimental arrangement and methods in § 3, and the

numerical methods in § 4. In § 5, we directly compare our experimental and numerical results for small excursion parameters with each other and with analytical predictions. We perform modal decompositions of this data in § 6. Then, in § 7, we present the results of investigations in which the excursion parameter was systematically increased, seeking to identify how modal decomposition is influenced by increased nonlinearity of the wave field. Finally, in § 8 we present our discussion and conclusions.

2. Linear theory

The far-field streamfunction generated by tidal flow over an isolated two-dimensional ridge in a linearly stratified finite-depth ocean is

$$\psi(X, Z, t) = U\,\mathrm{Real}\{\mathrm{e}^{-\mathrm{i}\omega_0 t}\,\phi\}, \tag{2.1}$$

where

$$\phi(X, Z) = \frac{h}{\pi}\sum_{n=1}^{\infty}\frac{\gamma_n}{n}\,\sin(nZ)\,\mathrm{e}^{\mathrm{i}nX}, \tag{2.2}$$

the tidal frequency is ω_0 and the magnitude of the barotropic tidal flow velocity in the far field is $U = \delta\,\omega_0$ (Pétrélis *et al.* 2006). The stretched non-dimensional vertical (Z) and horizontal (X) coordinates are defined in terms of their dimensional analogues x and z via

$$Z = \frac{\pi z}{h}, \qquad X = \frac{\pi x}{\mu h}, \tag{2.3}$$

in which

$$\mu = \frac{N}{\sqrt{\omega_0^2 - f^2}}, \tag{2.4}$$

the Coriolis frequency is f and the buoyancy frequency is N. The topography-dependent weight functions γ_n are the (complex) mode strengths for positive integer values of n.

For the purpose of comparison with our experiments, γ_n are calculated for an isolated, two-dimensional Gaussian ridge,

$$z_G = \begin{cases} \frac{\Lambda}{1-e^{-8}}\left[\exp\left(-\frac{x^2}{2\sigma^2}\right) - e^{-8}\right] & |x| \leqslant 4\sigma \\ 0 & |x| > 4\sigma \end{cases}, \tag{2.5}$$

where Λ is the ridge height and

$$\sigma = \frac{\Lambda}{e^{1/2}\,(1 - e^{-8})}, \tag{2.6}$$

so that the maximum topographic slope is 45°. This ridge is of compact, rather than infinite, horizontal extent because of the e^{-8} term. Such a restriction is necessary to guarantee a unique solution. We set

$$a = 2\sigma = \frac{2\Lambda}{e^{1/2}\,(1 - e^{-8})}, \tag{2.7}$$

as the characteristic half-width of the topography. The criticality parameter becomes

$$\varepsilon = \tan\Theta, \tag{2.8}$$

in which Θ, the angle of the wave beam to the vertical, is given by

$$\Theta = \cos^{-1}\sqrt{\frac{N^2 - f^2}{\omega_0^2 - f^2}} = \tan^{-1}\left(\frac{m_n}{k_n}\right), \tag{2.9}$$

and k_n and m_n are the horizontal and vertical wave numbers. By virtue of the rigid-lid boundary condition, m_n assumes the discrete values:

$$m_n = \frac{n\,\pi}{h}, \qquad n = 1,\ 2,\ 3, \ldots, \infty. \tag{2.10}$$

Whereas the theoretical solution given above is applicable for studying tidal conversion by topography on geophysical scales, three modifications must be considered for comparison with our laboratory measurements. First, the experiments are non-rotating, so that $f = 0$. Second, in our experiments ω_0 and N are of the same order of magnitude, so we retain non-hydrostatic terms by redefining the parameter μ of (2.4) as

$$\mu = \frac{\sqrt{N^2 - \omega_0^2}}{\omega_0}. \tag{2.11}$$

Finally, for our experiments the Reynolds number, $Re = U\,\Lambda/\nu$ (where ν is the kinematic viscosity), lies in the range $50 \leqslant Re \leqslant 850$. As such we include inside the sum of (2.2) a viscous damping factor

$$\exp\left\{-\frac{X\,\nu}{2\omega_0} n^3 \left(\frac{\pi}{h}\right)^2 \left[\frac{N^2}{N^2 - \omega_0^2}\right]^2\right\}. \tag{2.12}$$

The modified $\phi(X, Z)$ satisfies the viscous governing equations everywhere and the inviscid, no-normal flow condition at the boundaries. Therefore, the above damping factor is a viscous correction to the propagating wave field, but it does not remove singularities from the theoretical solution at the location of wave generation. As with the analyses of Lighthill (1978), Hurley & Keady (1997), Flynn, Onu & Sutherland (2003) and Peacock, Echeverri & Balmforth (2008), (2.12) provides aggressive damping of high vertical modes ($n \geqslant 4$).

Incorporating these considerations, the theoretical far-field vertical ($w = \partial\psi/\partial x$) and horizontal ($u = -\partial\psi/\partial z$) components of velocity are

$$w(X, Z, t) = \frac{U}{\mu}\,\mathrm{Real}\left\{\sum_{n=1}^{\infty} \gamma_n\, f_n \sin(nZ)\, \mathrm{e}^{\mathrm{i}\,(nXf_n - \omega_0 t + \pi/2)}\right\}, \tag{2.13}$$

and

$$u(X, Z, t) = -U\,\mathrm{Real}\left\{\sum_{n=1}^{\infty} \gamma_n \cos(nZ)\, \mathrm{e}^{\mathrm{i}\,(nXf_n - \omega_0 t)}\right\}, \tag{2.14}$$

respectively, where

$$f_n = 1 + \frac{\mathrm{i}\,\nu}{2\omega_0}\left(\frac{n\,\pi}{h}\right)^2 \left[\frac{N^2}{N^2 - \omega_0^2}\right]^2. \tag{2.15}$$

Note that for small n and non-vanishing μ, $\gamma_n\, f_n \simeq \gamma_n$ and thus in (2.13) the impact of viscosity is principally through the exponential term.

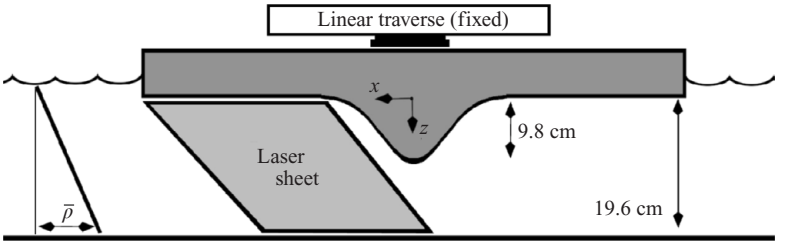

FIGURE 1. Schematic of the experimental set-up (front view). The topography is a foam Gaussian ridge of maximum height $\Lambda = 0.098 \pm 0.001$ m, mounted 'upside down' directly to a linear traverse.

3. Experimental set-up

Experiments were conducted in a 5.5 m × 0.69 m × 0.51 m glass wave tank. A linear salt-water stratification was established using Oster's 'double bucket' technique (Oster 1965). Three independent sets of experiments were conducted, for which we aimed to maintain a fixed stratification. The average buoyancy frequency was $N = 1.03 \pm 0.04\,\mathrm{rad\,s^{-1}}$, as measured using a calibrated precision measurement engineering (PME) conductivity probe, and verified by determining the wave beam angle for a known topographic oscillation frequency. Blocksom Filter matting was placed at both ends of the wave tank to effectively damp end-wall reflections.

Internal waves were generated by oscillating a two-dimensional rigid foam topography in the horizontal plane a millimetre or two below the free surface, as illustrated in figure 1. For the small variations in density considered here, this arrangement is equivalent, through a change of reference frame, to a fixed topography placed 'right-side up' with a tidal flow oscillating back and forth (Spiegel & Veronis 1960; Aguilar & Sutherland 2006). The styrofoam block, of total length 2.05 m, was cut into the shape of a Gaussian ridge with $\Lambda = 0.098 \pm 0.001$ m and a maximal topographic slope of $45.0^\circ \pm 1.5^\circ$. The channel depth far away from the ridge was $h = 0.196 \pm 0.001$ m, giving a depth ratio $\Lambda/h = 0.50 \pm 0.01$ that was held fixed for the experiments reported here. Internal wave generation by the free ends of the foam block was found to be insignificant.

The block was oscillated horizontally using a Parker linear traverse connected to LabVIEW. In the present study we were interested in the internal wave field response to changes in criticality and excursion. Thus, the forcing frequency and amplitude of oscillation were systematically varied. Peak-to-peak amplitudes were in the range $1.0 \times 10^{-3}\,\mathrm{m} \leqslant 2\delta \leqslant 35.0 \times 10^{-3}$ m, corresponding to excursion parameters $0.004 \leqslant \chi \leqslant 0.147$. To mitigate initialization transients, the amplitude of oscillation was ramped up to 99 % of its final value over five periods of oscillation (T), via the motion

$$x_t = \delta \sin(\omega_0 t)(1 - e^{-t/T_{spin}}), \tag{3.1}$$

where $T_{spin} = 7T/2\pi$. Recording of the experimental wave field was started $10T$ after the end of the ramp-up, at which point tests showed that the wave field was periodic. The fastest mode 1 signal generated during these experiments travelled at $c_{g,1} = 5.6 \pm 0.3\,\mathrm{cm\,s^{-1}}$ (where $c_{g,n} = Nh \sin^3 \Theta/n\pi$ is the horizontal group velocity of mode n) and had time to reach the end of the tank and reflect back into the field of view. The modal decomposition of wave fields before and after reflections could return into the field of view were consistent, however, confirming that the end-wall matting was effectively damping the reflections. The frequency ω_0 was selected such that the

wave beams propagated at angles to the vertical in the range $30^\circ \pm 2^\circ \leqslant \Theta \leqslant 60^\circ \pm 1^\circ$, corresponding to $0.57 \pm 0.05 \leqslant \varepsilon \leqslant 1.73 \pm 0.05$.

Particle image velocimetry (PIV) was used to measure the experimental velocity field. The stratified fluid was seeded with 10 μm glass spheres of typical density $1.03\,\mathrm{kg\,m^{-3}}$. These particles were visible when illuminated with a sheet of pulsating laser light from a class-4, ND-Yag Big Sky laser. As the internal waves propagated through the stratification, the motion of the particles was captured using a LaVision ImagerProX4M camera synchronized with the laser pulses and controlled via the LaVision DaVis imaging software. Experimental movies were captured at frame rates such that a snapshot of the velocity field was obtained 16, 32 or 64 times per period, with progressively finer time resolution selected as δ increased. Typical particle displacements between images were of the order of 10 pixels.

The measured wave field covered very nearly the entire vertical domain of the tank and a horizontal domain that spanned at least a 10 cm wide region within $0.17\,\mathrm{m} \leqslant x \leqslant 0.36\,\mathrm{m}$; $x = 0$ being the centre of the topography. Due to the bright reflection of the laser light on the top and bottom boundaries, there were narrow boundary regions (no wider than 8 mm) where particles could not be visualized and we were unable to obtain velocity measurements.

4. Numerical model

The two-dimensional numerical experiments were based on laboratory-scale numerical solutions of the non-hydrostatic equations of motion for a density-stratified fluid in the Boussinesq limit:

$$\frac{\partial \boldsymbol{u}}{\partial t} + \boldsymbol{u}\cdot\nabla\boldsymbol{u} + \hat{k}\frac{g}{\rho_0}\rho = -\frac{1}{\rho_0}\nabla p + \nu\nabla^2\boldsymbol{u} + \mathscr{F}_S + \hat{i}\mathscr{F}, \tag{4.1}$$

$$\frac{\partial \rho}{\partial t} + \boldsymbol{u}\cdot\nabla\rho = \kappa\nabla^2\rho, \tag{4.2}$$

$$\nabla\cdot\boldsymbol{u} = 0. \tag{4.3}$$

Here $\boldsymbol{u}$ is the velocity vector, ρ is the density deviation from the reference value ρ_0 and p is the pressure. The viscosity ν and diffusivity κ were both set to $10^{-6}\,\mathrm{m^2\,s^{-1}}$.

In contrast to the laboratory experiments, the Gaussian topography z_G was fixed in space and specified via the smooth function

$$z_G(x) = \Lambda e^{-\frac{1}{2}\left(\frac{x}{\sigma}\right)^2}, \tag{4.4}$$

where the parameters $\Lambda = 9.80\,\mathrm{cm}$ and $\sigma = 5.94\,\mathrm{cm}$ match the laboratory configuration. The surface $z_G(x)$ was immersed in a slightly extended computational domain $z \in [-\Delta, h]$ where $h = 19.7\,\mathrm{cm}$ as in the laboratory tank and Δ is a modelling parameter set to 10 % of h. No-slip boundary conditions were imposed on the flow at the immersed boundary. Below the immersed boundary the (non-physical) flow was held motionless. The upper boundary $z = H$ was taken as a free-slip rigid lid.

A uniform stratification matching the laboratory experiments was prescribed for a fluid initially at rest. A time-oscillating horizontal flow was excited for $t > 0$ via the body force $\mathscr{F}(t)$ in (4.1), which was consistent with the motion of the topography in (3.1):

$$\mathscr{F} = A\sin(\omega_0 t)\left(1 - e^{-t/T_{\mathrm{spin}}}\right). \tag{4.5}$$

The numerical values for A and ω_0 were set to match χ and ε in the laboratory experiments.

At the ends of the computational domain, $x = \pm L/2$, the stream-wise derivative $\partial/\partial x$ was set to zero for all fields. In general, waves propagating away from the sill crest would be reflected from such boundaries. To prevent this, an artificial damping term $\mathscr{F}_S(x, t)$ was used to gently damp the outward propagating waves as they approached the boundaries. These damping terms are only appreciably non-zero within regions of finite width adjacent to the boundaries. For example, the damping term in the vertical momentum equation near $x = -L/2$ was

$$-e^{-[(x+L/2)/\lambda]^2} w(x, z, t)/T_{damp}, \tag{4.6}$$

with the right boundary treated comparably. Similar terms were used to damp ρ while no explicit near-boundary damping is applied to either the streamwise component u or to p. The utility of the damping scheme was controlled by the width parameter λ and the damping time scale T_{damp}. Waves reflect from sponge regions that are too abrupt while excessively short damping time scales generate numerical instabilities. Preliminary experiments were run varying the domain size L along with the damping parameters to determine reasonable choices. For the numerical experiments reported, $L = 5\,\mathrm{m}$, $\lambda = 5\sigma$ and $T_{damp} = 0.1\,\mathrm{s}$.

The spatial discretization was held fixed across the different experiments with $nx = 10239$ and $nz = 513$, corresponding to grid spacings of $\mathrm{d}x \approx 0.488\,\mathrm{mm}$ and $\mathrm{d}z \approx 0.4275\,\mathrm{mm}$ in the horizontal and vertical, respectively. The grid spacings were chosen to ensure at least two grid points within the nominal viscous boundary layer over the topography, which has an approximate scale $\sqrt{\nu/\omega_0} \approx 1.0 - 1.4\,\mathrm{mm}$; and $\mathrm{d}x$, $\mathrm{d}z$ were of comparable size because the ridge has a maximum slope of 45°. The time step varied between experiments. For the smallest values of χ, $\mathrm{d}t$ was set to 1/512 of the forcing period, and this decreased linearly with increasing χ. The use of an immersed boundary within a vertically extended computational domain, coupled with the isolation of the lateral boundaries via damping terms permits expansion of unknowns in terms of odd and even Fourier series. Raw results were subsampled and time averaged to match the spatial and temporal resolution inherent in the PIV measurements in the laboratory.

5. Results for small excursion

Figures 2(*a*) and 2(*d*) show, respectively, experimental velocity fields for subcritical ($\varepsilon = 0.70 \pm 0.04$) and supercritical ($\varepsilon = 1.73 \pm 0.05$) topographies with $\chi = 8.4 \times 10^{-3}$. The velocity fields are presented in the frame of reference in which the topography is stationary and the phase of tidal forcing $\Omega = 0°$, corresponding to the maximum tidal flow in the positive x direction. Colours and arrows indicate, respectively, the magnitude and direction of the perturbation velocity field normalized by the far-field tidal velocity. Blank regions demarcate areas that were either outside of the camera's field of view or obscured by laser reflections. Figures 2(*b*) and 2(*e*) present the corresponding numerical wave fields, and figures 2(*c*) and 2(*f*) the corresponding far-field theoretical solutions (2.13) and (2.14). The experimental data was obtained in regions of constant depth away from the topography, and the theoretical data, which is only formally valid in the far field, is shown for the same domain. The numerical snapshots are presented for a larger horizontal domain since the data was readily available.

For the subcritical case, illustrated in figure 2(*a–c*), away from the ridge a single dominant wave beam propagates to the right at an angle $\Theta = 35° \pm 2°$. Near the ridge (figure 2*b*), we also see a left-propagating wave beam generated over the

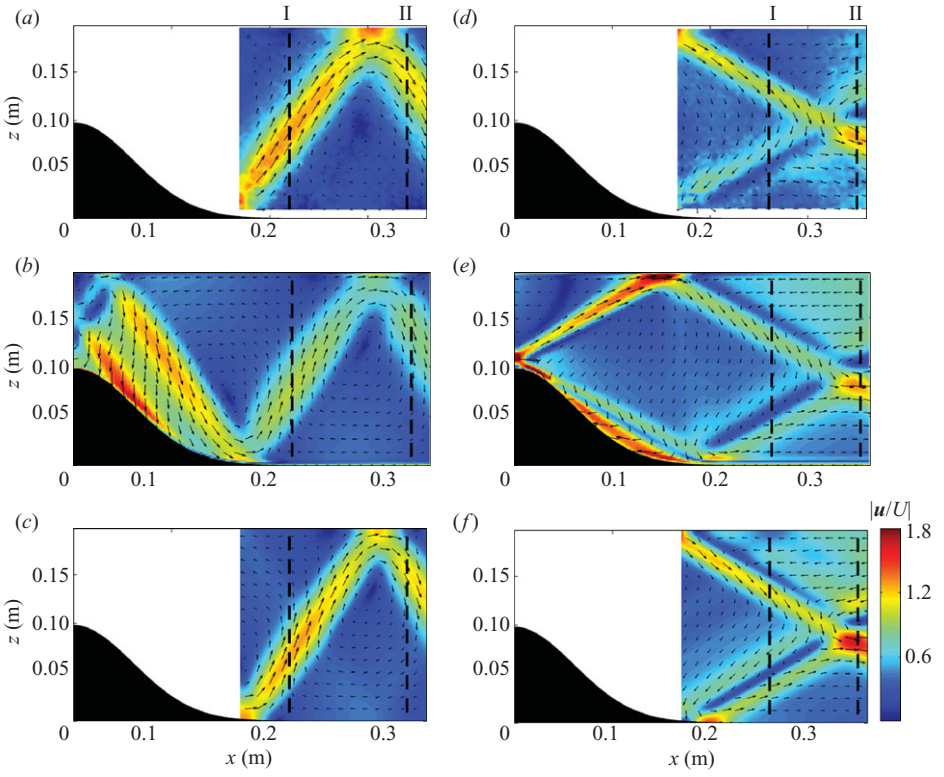

FIGURE 2. Snapshots of the velocity perturbation $\boldsymbol{u}/U$ to the far-field barotropic tide, with $\varepsilon = 0.70 \pm 0.04$ (*a–c*) and $\varepsilon = 1.73 \pm 0.05$ (*d–f*). Experimental, numerical and theoretical results are shown, respectively, in the top, middle and bottom rows. Colours and arrows indicate the instantaneous magnitude and direction of velocity. I and II indicate vertical cross-sections where direct comparisons are made in figure 3.

right-side slope. For the supercritical case illustrated in figures 2(*d–f*), a pair of internal wave beams propagate to the right and both up and down with $\Theta = 60° \pm 1°$.

For both the sub- and supercritical cases, the form of the wave beams agrees for experiments, numerics and theory. The simulated wave fields are a little weaker than the experimental observations, however, and in the supercritical case the theoretical wave field is a little stronger. We attribute the latter to the fact that, despite our viscous correction of (2.12), the theoretical supercritical solution generates a singular wave field at the critical slope; an aspect of the theory that is not present in the experiments or simulations. The present results are consistent with previous studies in which theory often slightly overpredicts the peak strength of wave beams as compared to experiments (Flynn *et al.* 2003; Zhang, King & Swinney 2007 and Peacock *et al.* 2008).

In figure 3, we show vertical cross-sections of the vertical velocity w at locations I and II indicated in figure 2. These profiles are presented at two different phases of the tidal oscillation in figures 3(*a–d*) for the subcritical case; and in figures 3(*e–h*) for the supercritical case. The experimental profiles were averaged over 17 cycles to reduce the effect of experimental noise. Good agreement between the theory (solid curves), experiment (dashed curves) and numerics (dotted curves) is generally observed. The supercritical profiles, for example, are in particularly close agreement at $\Omega = 90°$

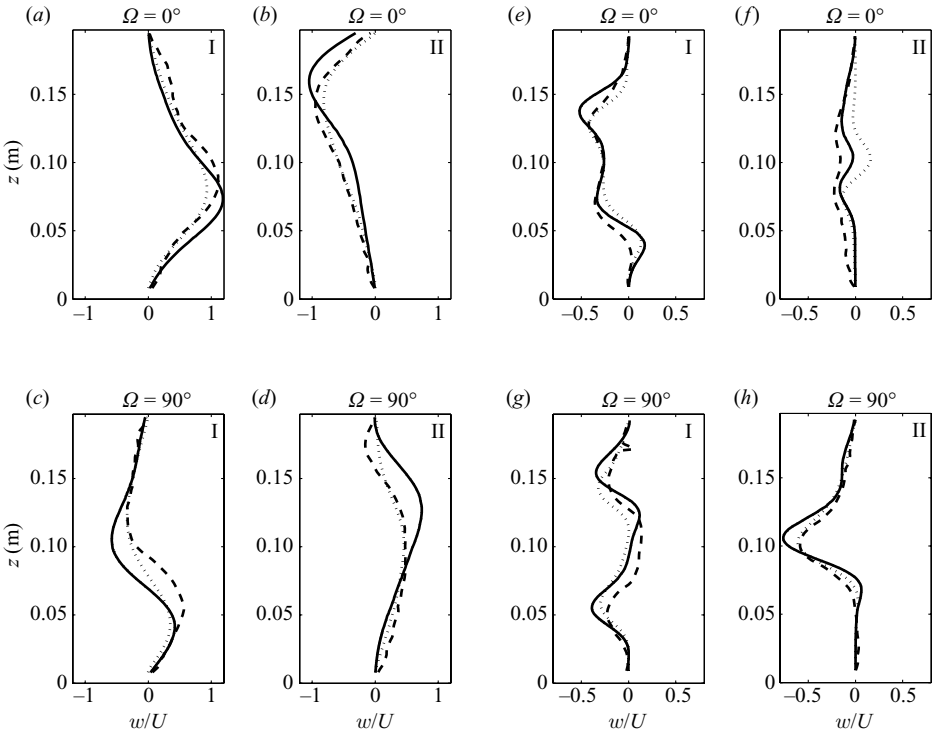

FIGURE 3. Cross-sections of the vertical velocity field w/U for $\varepsilon = 0.70 \pm 0.04$ (*a–d*) and $\varepsilon = 1.73 \pm 0.05$ (*e–h*). Panels in a column are taken at the same cross-section, respectively (from left to right): I and II for the subcritical wave field and I and II for the supercritical wave field. Cross-sections I and II are defined in figure 2. The lines correspond to the theoretical solution (solid), experimental data (dashed) and numerical data (dotted).

(figure 3*h*), with the theoretical peak a little stronger and sharper. In some other comparisons, however, the agreement is weaker. For the subcritical case at $\Omega = 90°$ (figure 3*c*), for example, theory predicts a strong downward flow at mid-depth, below which there is a quick reversal to an upward flow. In contrast, the experiments reveal a weaker downward flow at mid-depth, below which there is a stronger upward flow. The numerical results lie in between. We investigated possible reasons for these discrepancies: (i) uncertainty in the phase of the experimental wave fields, which were sampled at 16 frames per cycle; and (ii) uncertainty in the criticality parameter and depth ratio of the experiments. Neither of these, however, could account for the observed errors. As our later studies show, the discrepancies are associated with differences in the high-mode content of the wave field.

These spatial comparisons are complemented by temporal comparisons presented in figure 4. Figures 4(*a–c*) and 4(*e–f*) show experimental, numerical and theoretical time-series for the vertical velocity profiles at location I, for the sub- and supercritical experiments, respectively. The corresponding depth-averaged Fourier spectra of the experimental and the numerical data, obtained using either 17 or 18 tidal cycles, are presented in figures 4(*d*) and 4(*h*). Not surprisingly, in both cases strong peaks are observed at the fundamental frequency ω_0, where experiments and numerics agree to within 3.5 % for the subcritical case and 2.7 % for the supercritical case. Higher harmonics $2\omega_0$ and $3\omega_0$, which are evanescent for these experiments, are of relatively

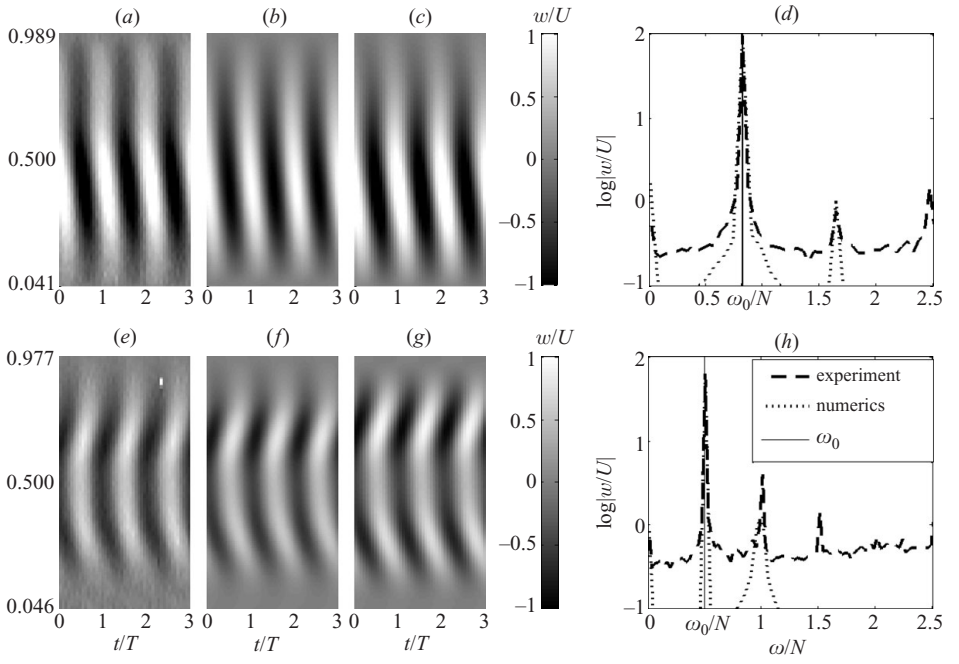

FIGURE 4. Vertical time-series and depth-averaged Fourier spectra of w/U at cross-section I (see figure 2). Time-series from (a) experiments, (b) simulations and (c) theory for $\varepsilon = 0.70 \pm 0.04$; and ($d$) corresponding depth-averaged spectra. Time-series from (e) experiments, (f) simulations and (g) theory for $\varepsilon = 1.73 \pm 0.05$; and ($h$) corresponding depth-averaged spectra.

small amplitude, indicating that the wave field is dominated by waves of frequency ω_0 and can be reasonably considered linear. Similar qualitative results (not shown) were found at location II.

6. Modal decomposition

6.1. *Implementation*

One can recover mode strengths $\gamma_n = |\gamma_n| \, \mathrm{e}^{\mathrm{i}\phi_n}$ from vertical velocity measurements such as those presented in the previous section. We first select a horizontal location and absorb $\mathrm{Real}(n\,X\,f_n) = n\,X$ and the phase shift of $\pi/2$ in (2.13) into a phase function $\hat{\phi}_n = \phi_n + n\,X + \pi/2$. Projecting the vertical velocity profile onto the sinusoidal vertical basis modes of the linear stratification yields

$$\bowtie_n \equiv \int_0^{\pi} w \sin(nZ)\,\mathrm{d}Z = \left(\frac{\pi U}{2\mu}\right) |\gamma_n| \, \mathrm{e}^{-n\,X\,\mathrm{Imag}(f_n)} \, \mathrm{Real}\{ f_n \, \mathrm{e}^{\mathrm{i}(\hat{\phi}_n - \omega_0 t)} \}\,. \tag{6.1}$$

Equation (6.1) can be solved for $|\gamma_n|$ by multiplying by $\cos(\theta_n - \omega_0 t)$ and choosing the value of θ_n that maximizes the integral

$$\frac{2}{t_{max}} \int_0^{t_{max}} \bowtie_n \cos(\theta_n - \omega_0 t)\,\mathrm{d}t\,, \tag{6.2}$$

where t_{max} consists of a complete number of wave periods associated with the fundamental frequency ω_0. The critical values of θ_n give the phases ϕ_n for the corresponding vertical modes.

Equation (6.2) filters internal waves of frequency $2\omega_0$, $3\omega_0$, etc. which arise at the generation site (Lamb 2004; Legg & Huijts 2006) and at points of wave beam intersection or reflection (Peacock & Tabaei 2005; Tabaei, Akylas & Lamb 2005). Although (6.2) does not remove inter-harmonic internal waves, for our small-amplitude experiments these were at least an order of magnitude smaller than the harmonic frequencies (see figure 4 and also figures 8 and 9 of Legg & Huijts 2006).

As indicated by the results in figures 2(*a*) and 2(*d*), the bottom 4 % and top 2 % of the experimental images were inaccessible because of laser sheet reflections. Strictly speaking, the standard Fourier decomposition of (6.1) cannot be applied because the trigonometric basis functions are not orthogonal over the truncated vertical domain. Consequently, non-orthogonal Fourier series integrals are employed:

$$\int_{\pi\alpha/h}^{\pi(h-\beta)/h} w \sin(nZ)\,\mathrm{d}Z = \sum_{m=1}^{\infty} \Upsilon_{mn}\,\psi_m. \tag{6.3}$$

Here α and β reflect the degree of image loss near $z=0$ and $z=h$, respectively, and the modal matrix Υ_{nm} is

$$\Upsilon_{nm} = \int_{\pi\alpha/h}^{\pi(h-\beta)/h} \sin(nZ)\sin(mZ)\,\mathrm{d}Z, \tag{6.4}$$

leaving

$$\psi_m = \frac{U}{\mu}|\gamma_m|\,\mathrm{e}^{-m\,X\,\mathrm{Imag}(f_m)}\,\mathrm{Real}\{f_m\,\mathrm{e}^{\mathrm{i}(\hat{\phi}_m-\omega_0 t)}\}. \tag{6.5}$$

Equation (6.3) represents a system of n linear equations, which can be solved for $\{|\gamma_m|,\ \phi_m\}$. As Υ_{nm} is diagonally dominant for reasonable choices of α and β, the infinite series of (6.3) was satisfactorily truncated after ten terms.

Since $w \to 0$ as the ray slope becomes horizontal, the signal-to-noise ratio was small in experiments with $\Theta \gtrsim 60^\circ$, which restricted our ability to extract modal amplitudes for highly supercritical topography. In principle, one could also obtain estimates of $|\gamma_n|$ and ϕ_n from measurements of the horizontal velocity field. However, owing to the different trigonometric basis functions (i.e. $\cos(nZ)$ versus $\sin(nZ)$), we found that estimates of the mode strengths obtained using u were much more susceptible to image loss and to thin boundary layers that, in the experiment, impose a no-slip boundary condition on both surfaces.

For the results presented in § 6.2, we accepted only data for which consistent measurements of both $|\gamma_n|$ and ϕ_n were obtained across the entire horizontal domain of the experiment. Instances of inconsistent data were rare and did not arise in repeat experiments for linear internal waves and vertical modes $n=1,\ 2$ and 3. On the other hand, it was difficult to obtain consistent results for $n \geqslant 4$ from both experiments and numerics. One reason for this is that, as discussed in § 2, viscous damping impacts high modes much more significantly than low modes. While this effect can be accounted for theoretically (e.g. by normalizing measured mode strengths by the exponential term of (2.12)), this requires dividing by small quantities and leads to non-trivial absolute errors. In light of these observations and the conclusions of Di Lorenzo *et al.* (2006) that 'radiated energy is [most] heavily concentrated' in the low vertical modes, we focus on the vertical modes $n=1,\ 2$ and 3.

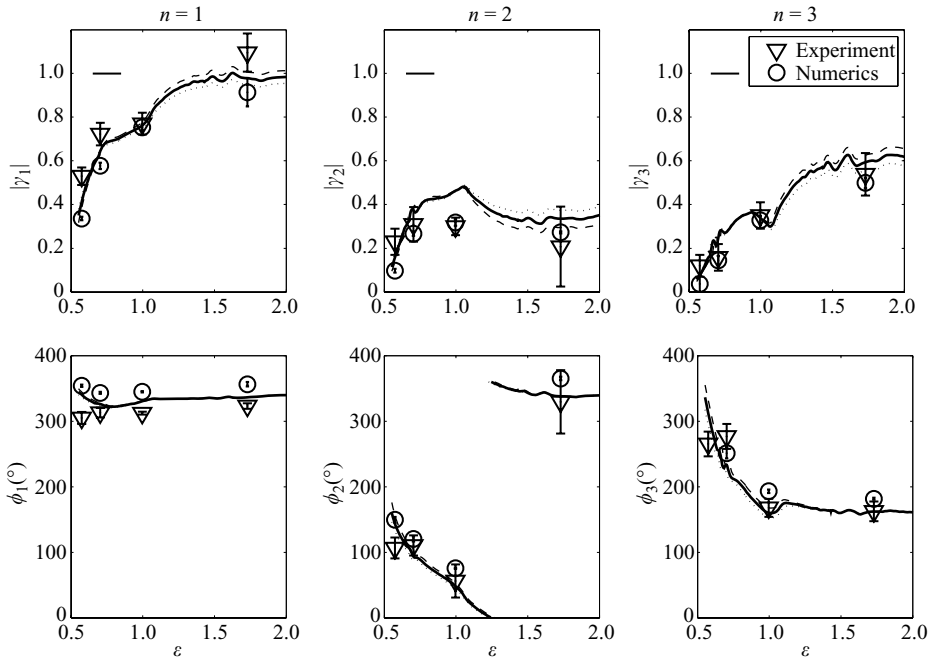

FIGURE 5. Modal amplitudes and phases for $n=1$, 2 and 3 with $\Lambda/h=0.50\pm0.01$ and $\chi\leqslant1.68\times10^{-2}$. The theoretical solution is given by the dotted ($\Lambda/h=0.49$), solid ($\Lambda/h=0.50$) and dashed ($\Lambda/h=0.51$) lines. The horizontal lines shown in the upper left hand corner of the top three panels indicate typical errors in ε.

6.2. *Application to experimental and numerical data*

Figure 5 shows modal amplitudes and phases for $n=1$, 2 and 3 as a function of ε for experiments (triangles) and numerics (circles). Horizontal error bars reflect representative errors in ε for the laboratory experiments and vertical error bars reflect measurement variations in sampling at 20 evenly spaced horizontal locations (and in some cases multiple experiments), covering at least 0.10 m in the range $0.17\,\mathrm{m}\leqslant x\leqslant0.36\,\mathrm{m}$. Superimposed are the theoretical solutions derived from Pétrélis *et al.* (2006); the thin curves indicate the uncertainty in the depth ratio to which supercritical modal amplitudes are quite sensitive. The theoretical curves are not, in general, smooth functions because the system of linear equations whose solution specifies γ_n contains a matrix (different from the diagonally dominant matrix Υ_{nm} of (6.4)) that may become ill-conditioned for select choices of ε. Hence, small-scale noise is introduced that does not diminish as the number of modes (i.e. the resolution) is increased. Notwithstanding these distractions, the agreement between theory and experiment is good, almost always falling within the scale of the horizontal and vertical error bars. There is, furthermore, favourable agreement with results obtained from applying the modal decomposition algorithm to the numerical results. A couple of minor discrepancies exist: for example, ϕ_1 is consistently higher for the numerical as compared to the theoretical and experimental data. On the other hand, there are cases where experiment and numerics closely agree on a result that is different from theory: for example, for $|\gamma_2|$ at the critical case $\varepsilon=1.00\pm0.04$.

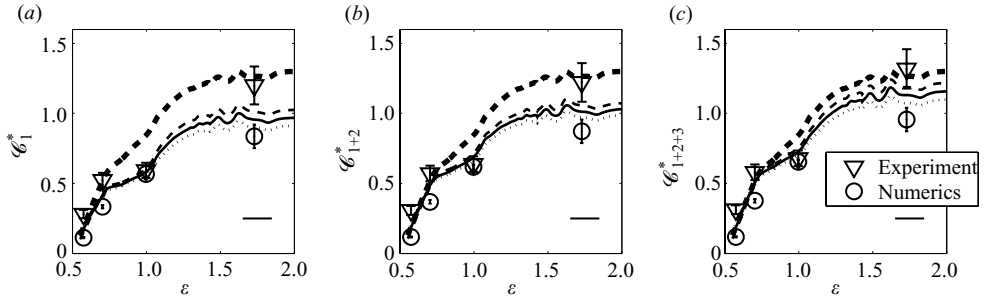

FIGURE 6. Non-dimensional tidal power converted into baroclinic low modes: (*a*) mode 1 ($\mathscr{C}^*_1$), (*b*) modes 1 and 2 ($\mathscr{C}^*_{1+2}$) and (*c*) modes 1 through 3 ($\mathscr{C}^*_{1+2+3}$) versus ε. The thin lines correspond to the model solution with $\Lambda/h = 0.49$ (dotted), $\Lambda/h = 0.50$ (solid) and $\Lambda/h = 0.51$ (dashed). The thick dashed line (which is identical in the three panels) shows the approximate total predicted energy conversion rate for $\Lambda/h = 0.50$, obtained by truncating the sum in (6.6) after 20 terms. Data points and error bars are as indicated in figure 5.

6.3. *Linear energy flux*

The rate of energy conversion can be calculated from experimental and numerical estimates of the mode strengths. More specifically, by adapting (2.31) of Pétrélis *et al.* (2006) to a non-hydrostatic wave field, it can be shown that

$$\mathscr{C}^* = \sum_{n=1}^{\infty} \frac{\gamma_n \bar{\gamma}_n}{n} = \frac{2\pi\mathscr{C}}{\rho U^2 h^2 \sqrt{N^2 - \omega^2}}, \tag{6.6}$$

where the overbar indicates a complex conjugate, $\mathscr{C}$ is the total converted tidal power, measured in Watts per unit ridge length and $\mathscr{C}^*$ is the corresponding non-dimensional result. By truncating the series of (6.6), we can determine the non-dimensional tidal power converted into, say, mode 1 ($\mathscr{C}^*_1$); modes 1 and 2 ($\mathscr{C}^*_{1+2}$); or modes 1, 2 and 3 ($\mathscr{C}^*_{1+2+3}$). Figures 6 (*a*) to (*c*) respectively show $\mathscr{C}^*_1$, $\mathscr{C}^*_{1+2}$ and $\mathscr{C}^*_{1+2+3}$ as functions of ε. The energy conversion increases with ε, a trend that is supported by both the experimental (triangles) and numerical (circles) results. Most of the energy content is contained in mode 1. The agreement between measurement and theory is very good for wave fields over subcritical and critical topography; there is a more noticeable discrepancy for the supercritical case that is associated with the differences in the amplitude of mode 1 reported in figure 5. Overall, the level of agreement is on a par with the analysis of Di Lorenzo *et al.* (2006), who compared theoretical tidal conversion rates against the output of a hydrostatic regional ocean modelling System (ROMS) simulation.

7. Results for larger excursion

While there is good agreement between experiment, theory and numerical simulation thus far, we find evidence of nonlinear effects even for small excursion parameters ($\chi \leqslant 1.68 \times 10^{-2}$). The frequency spectra in figures 4(*d*) and 4(*h*), for example, show higher harmonics that are not accounted for by a linear model. We therefore systematically increased the excursion parameter by an order of magnitude or more to enhance nonlinearity in the experiments and simulations, and studied the impact on the radiated modal structure. Starting with $\chi = 0.0084$, for subcritical topography we increased the excursion to $\chi = 0.084$; and for supercritical topography we increased to

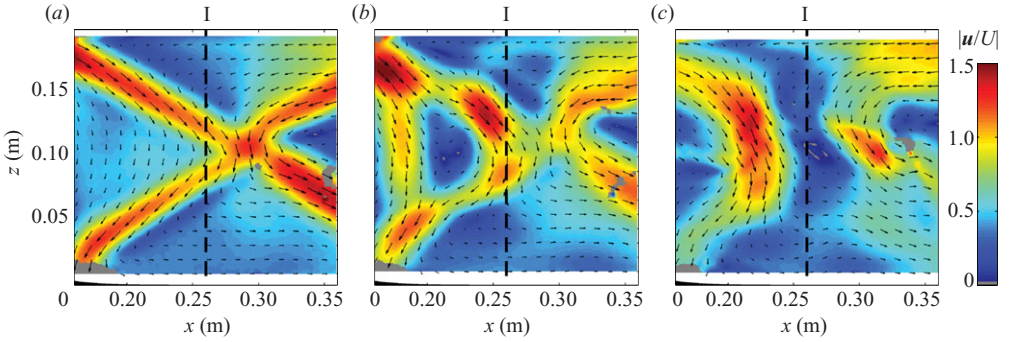

FIGURE 7. Experimental snapshots of the velocity perturbation $|\boldsymbol{u}/U|$ for $\varepsilon = 1.73 \pm 0.05$ and (*a*) $\chi = 0.042$, (*b*) $\chi = 0.084$, (*c*) $\chi = 0.147$.

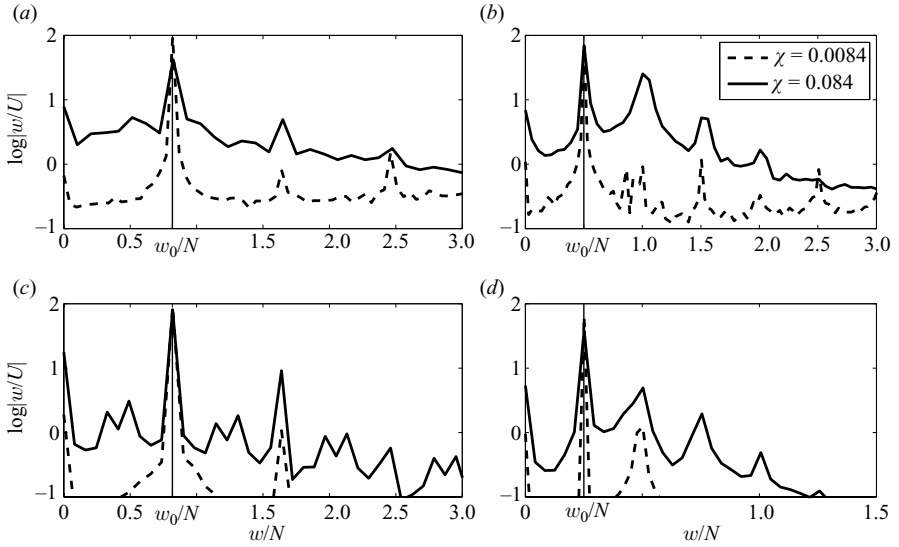

FIGURE 8. Depth-averaged Fourier spectra of w at location I in experiments with (*a*) $\varepsilon = 0.70 \pm 0.04$ and (*b*) $\varepsilon = 1.73 \pm 0.05$; results for the corresponding simulations are presented in (*c*) and (*d*). The lines show spectra for $\chi = 0.0084$ (dashed) and $\chi = 0.084$ (solid); as well as the location of ω_0/N (thin solid).

$\chi = 0.168$. For these larger values of χ, the coherent far-field wave beam pattern broke down, as shown in figure 7. Associated with this, qualitative observations indicated that the flow was no longer laminar over the top of the topography.

The signature of this nonlinear activity can be seen in the frequency content of the radiated wave field. In figure 8 we present depth-averaged Fourier spectra of the experimental and numerical vertical velocity fields at location I. For $\chi = 0.0084$, harmonic peaks are over an order of magnitude smaller than the peaks at the fundamental frequency. For $\chi = 0.084$, the relative magnitude of harmonic peaks increases significantly; for instance, the power at the first harmonic becomes almost half of the power at the fundamental frequency for the supercritical experiment. Note that all the harmonics are either evanescent or at best vertically propagating (i.e. the first harmonic for $\varepsilon = 1.73 \pm 0.05$), so they are confined to the neighbourhood where they are generated. The spectra shown in figure 8, therefore, do not contain

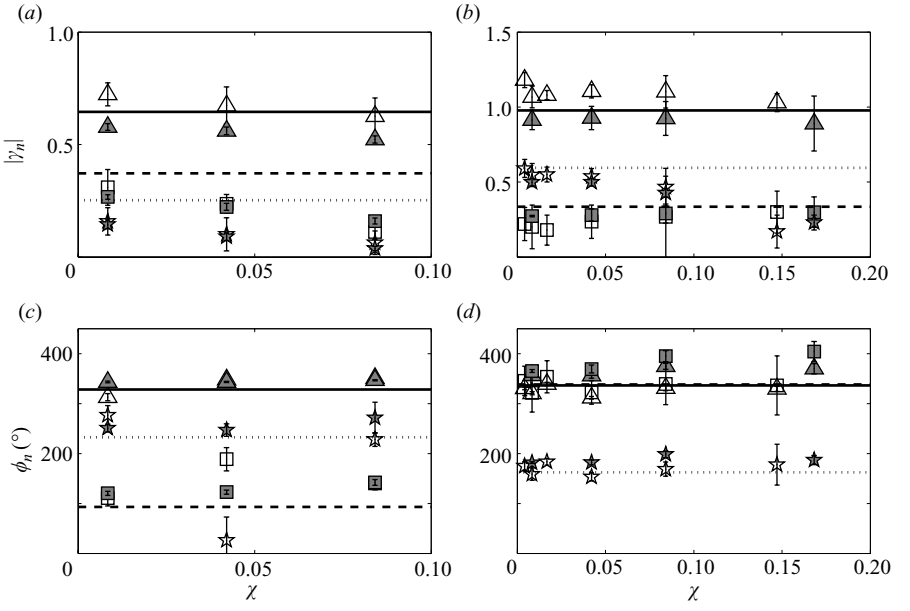

FIGURE 9. Variation of the modal decomposition results with χ for (a, c) $\varepsilon = 0.70 \pm 0.04$ and (b, d) $\varepsilon = 1.73 \pm 0.05$. Data point markers are as follows: $|\gamma_1|$, triangles; $|\gamma_2|$, squares; and $|\gamma_3|$, stars. Open and closed data points show experimental and numerical results, respectively. Horizontal lines show linear theoretical estimates for modes 1 (solid), 2 (dashed) and 3 (dotted).

harmonics directly excited by the topography (Bell 1975), but instead generated through nonlinearities, most likely at nearby wave beam reflections or crossings (Peacock & Tabaei 2005; Tabaei *et al.* 2005; Legg & Huijts 2006; Korobov & Lamb 2008). The relative amplitude of the inter-harmonic content also increases with χ, although it remains weaker than the harmonic peaks. An interesting feature in the spectra of the numerical subcritical wave field is the presence of well-defined sub- and inter-harmonic peaks. The sum of the frequencies of the two subharmonic peaks is equal to the fundamental frequency; and the frequencies of the inter-harmonic peaks are equal to either the fundamental or a harmonic frequency plus the frequency of one of the subharmonic peaks. Korobov & Lamb (2008) also report on such 'self-similar' spectra, and attribute the subharmonic peaks to a subharmonic parametric instability and the inter-harmonic peaks to wave–wave interactions. These peaks are not present in the experimental data, however, which contains a smoother distribution of inter-harmonic content, with amplitude comparable to the amplitudes of the subharmonic peaks in the numerical wave field.

In figure 9 we present modal decomposition amplitude and phase results for the sub- and supercritical topography as a function of χ. We first consider the supercritical results in figures 9(b) and 9(d). Even up to the largest excursion parameter, the modal decomposition method measured a consistent mode 1 structure across the interrogation region from both experimental and numerical data, as indicated by the small error bars. There is a small decrease of $|\gamma_1|$ with χ (at most 10 %, but typically a lot less) for excursion parameters approaching $\chi = 0.168$. The mode 1 phase, ϕ_1, is also hardly affected. We were also able to reliably measure amplitudes and phases for modes 2 and 3. As with mode 1, an order of magnitude increase in χ yields little change in $|\gamma_2|$ or ϕ_2. There is a more substantial variation ($\sim$ 50 %) in $|\gamma_3|$, but $|\phi_3|$ is not noticeably affected.

Results for subcritical topography, presented in figures 9(*a*) and 9(*c*), reveal a slightly more noticeable effect on $|\gamma_1|$; but even so, this decreases by only 10 % in simulations and 15 % in experiments. The measured amplitudes $|\gamma_2|$ and $|\gamma_3|$ also monotonically decrease with increasing excursion parameter. As with the supercritical results, for both experiments and numerical simulations the mode 1 phase is weakly influenced by the increasing excursion parameter, and agrees well with theory. There is some scatter in the phase measurements of modes 2 and 3 for $\chi = 0.042$. We repeated this particular experiment and observed the same result, showing it was robust, although notably different from numerics.

8. Discussion and conclusions

We have performed the first laboratory investigations of internal tide generation by a two-dimensional ridge in a finite-depth and continuously stratified ocean. In doing so, we developed and implemented a method to extract modal amplitudes from experimental PIV data, accounting for practical difficulties such as incomplete information in the vertical domain. This modal decomposition is a useful tool for characterizing the structure of an internal tide, and furthermore provides a means for estimating the linear energy flux. Our results presented in § 5 and § 6 demonstrate good agreement between experiments, numerics and linear theory for the low-mode structure of internal tides generated by sub- and supercritical topography in the limit of a small excursion parameter.

Small discrepancies do arise even in the linear regime, however. These are manifest as weak harmonics in the frequency spectra, and more obviously in comparisons of vertical velocity profiles, in figure 3. These discrepancies cannot be accounted for by the small uncertainties in our experimental parameters; we checked this by computing the analytical solution for values of ε and Λ/h within error ranges. Our modal decomposition results reveal that the observed discrepancies are not associated with the low modes, for which there is agreement between experiment, theory and numerics. Our conclusion, therefore, is that there is a mismatch of measured and predicted modes for $n \geqslant 4$, which are the modes responsible for the fine scale features of wave beams. This issue is difficult to probe in experiments because significant viscous damping of high modes prevents us from reliably extracting the corresponding modal amplitudes. Moreover, in critical and supercritical regimes linear theory is singular, which is unphysical. We note that these small discrepancies have a minimal effect on the measured and predicted energy flux for the canonical topographic configuration considered (as shown in figure 6), consistent with observations by Di Lorenzo *et al.* (2006) and Pétrélis *et al.* (2006) that the high modes do not significantly impact the energy flux away from topography, which is dominated by the low modes, and principally mode 1.

As the excursion increases to 15 % of the width of the ridge, the coherent wave beam structure ultimately disappears. This is accompanied by a noticeable increase in the harmonic and inter-harmonic content of the wave field. Remarkably, this nonlinear activity has little impact on the amplitude and phase of the radiated mode 1 tide. There is a more noticeable effect for mode 2 and even more so for mode 3; namely, a steeper decrease in amplitude and some scatter in the phase of the subcritical experiments. This suggests that nonlinear processes first influence the medium-scale dynamics associated with the finer vertical scales of modes 2 and 3. All modal amplitudes decrease with increasing χ, indicating that energy is drawn from the internal tide at the fundamental frequency.

Since mode 1 transports most of the energy away from the topography, and its relative amplitude is little affected by increasing χ, we conclude that the energy radiated away from the topography in these experiments is not significantly influenced by nonlinear processes. This new insight reveals that the linear theory of Pétrélis *et al.* (2006) reasonably predicts tidal conversion even for finite excursion parameters where nonlinearities start to become evident, and is useful for the parameterization of internal tide generation by topography with large depth ratios, such as Hawaii. On the other hand, for a small and narrow topographic feature the internal wave response is dominated by higher modes, as reported by Legg & Huijts (2006). As such, in this 'low-narrow' regime, we expect the influence of nonlinearities to be felt at comparably smaller excursion parameters.

There are, of course, differences between our experiments and the ocean; which must be considered when trying to extrapolate these results. For practical reasons we did not incorporate background rotation into the experiments, but this plays a minimal role for most ocean generation problems, except near-critical latitudes where the parametric subharmonic instability may be a first-order part of the response. We also accounted for the impact of viscous dissipation in the laboratory, which was negligible ($\sim$1 %) for mode 1. Other notable differences, however, merit further discussion. One concerns the fact that higher harmonics in our system are either vertically propagating or evanescent and therefore do not transport energy away from their point of generation. In contrast, in the ocean there is a multitude of propagating higher harmonics. We were unable to access this regime in our experiments due mainly to signal-to-noise issues at low beam angles. The lack of propagating harmonics in the experiments has the benefit, however, of being able to clearly identify whether the harmonics observed are generated directly by the topography (Bell 1975; Lamb 2004), or by wave–wave interactions away from the topography (Peacock & Tabaei 2005; Legg & Huijts 2006). We found significant harmonic content of the wave field that could only have been generated in the far field.

Overall, our results support the use of linear models for predicting tidal conversion rates even in transitional regimes with finite excursion parameter up to 15 %, providing a useful guide for ocean modelling. An important issue for future experimental studies is to investigate a non-uniform background stratification. In this case we anticipate that the smaller scale structures of mode 1, which are localized in the vicinity of the thermocline, could be more strongly impacted by nonlinear activity close to the topography. Similarly, wave fields generated by smaller scale topographic features will be dominated by higher-modes, and our experimental results indicate that nonlinearities have a bigger impact in this regime.

The authors are grateful to Damon L. Vander Lind for assistance with the experimental apparatus and the modal decomposition algorithm, and Professor Neil J. Balmforth, who provided the initial algorithm to plot the theoretical solutions. Financial support was generously provided by the Office of Naval Research under grants N00014-08-0390 and N00014-05-1-0573, and by the National Science Foundation under grants OCE 0645529 and OCE 04-25283. Partial support for MRF was generously provided by NSERC through the Discovery Grant Program.

REFERENCES

Aguilar, D. A. & Sutherland, B. R. 2006 Internal wave generation from rough topography. *Phys. Fluids* **18**, 066603.

Bell, T. H. 1975 Lee waves in stratified flows with simple harmonic time dependence. *J. Fluid Mech.* **67**, 705–722.

Di Lorenzo, E., Young, W. R. & Llewellyn Smith, S. G. 2006 Numerical and analytical estimates of M2 tidal conversion at steep oceanic ridges. *J. Phys. Oceanogr.* **36**, 1072–1084.

Egbert, G. D. & Ray, R. D. 2000 Significant dissipation of tidal energy in the deep ocean inferred from satellite altimeter data. *Nature* **405**, 775–778.

Flynn, M. R., Onu, K. & Sutherland, B. R. 2003 Internal wave generation by a vertically oscillating sphere. *J. Fluid Mech.* **494**, 65–93.

Garrett, C. & Kunze, E. 2007 Internal tide generation in the deep ocean. *Annu. Rev. Fluid Mech.* **39**, 57–87.

Hurley, D. G. & Keady, G. 1997 The generation of internal waves by vibrating elliptic cylinders. Part 2. Approximate viscous solution. *J. Fluid Mech.* **351**, 119–138.

Korobov, A. S. & Lamb, K. G. 2008 Interharmonics in internal gravity waves generated by tide-topography interaction. *J. Fluid Mech.* **611**, 61–95.

Kunze, E. & Llewellyn Smith, S. G. 2004 The role of small-scale topography in turbulent mixing of the global ocean. *Oceanography* **17**, 55–64.

Lamb, K. G. 2004 Nonlinear interaction among internal wave beams generated by tidal flow over supercritical topography. *Geophys. Res. Lett.* **31**, L09313.

Legg, S. & Huijts, K. M. H. 2006 Preliminary simulations of internal waves and mixing generated by finite amplitude tidal flow over isolated topography. *Deep-Sea Res.* II **53**, 140–156.

Lighthill, M. J. 1978 *Waves in Fluids*. Cambridge University Press.

Llewellyn Smith, S. G. & Young, W. R. 2003 Tidal conversion at a very steep ridge. *J. Fluid Mech.* **495**, 175–191.

Nash, J. D., Alford, M. H. & Kunze, E. 2005 Estimating internal wave energy fluxes in the ocean. *J. Atmos. Ocean. Technol.* **22**, 1551–1570.

Oster, G. 1965 Density gradients. *Sci. Am.* **213**, 70–76.

Peacock, T., Echeverri, P. & Balmforth, N. J. 2008 An experimental investigation of internal tide generation by two-dimensional topography. *J. Phys. Oceanogr.* **38**, 235–242.

Peacock, T. & Tabaei, A. 2005 Visualization of nonlinear effects in reflecting internal wave beams. *Phys. Fluids* **17**, 061702.

Pétrélis, F., Llewellyn Smith, S. G. & Young, W. R. 2006 Tidal conversion at a submarine ridge. *J. Phys. Oceanogr.* **36**, 1053–1071.

Ray, R. D. & Mitchum, G. T. 1997 Surface manifestation of internal tides in the deep ocean: osbservations from altimetry and island gauges. *Prog. Oceanogr.* **40**, 135–162.

Rudnick, D. L., Boyd, T. J., Brainard, R. E., Carter, G. S., Egbert, G. D., Gregg, M. C., Holloway, P. E., Klymak, J. M., Kunze, E., Lee, C. M., Levine, M. D., Luther, D. S., Martin, J. P., Merrifield, M. A., Moum, J. N., Nash, J. D., Pinkel, R., Rainville, L. & Sanford, T. B. 2003 From tides to mixing along the Hawaiian ridge. *Science* **301**, 355–357.

Simmons, H. L., Hallberg, R. W. & Arbic, B. K. 2004 Internal wave generation in a global baroclinic tide model. *Deep-Sea Res.* II **51**, 3043–3068.

Spiegel, E. A. & Veronis, G. 1960 On the Boussinesq approximation for a compressible fluid. *Astrophys. J.* **131**, 442–447.

St. Laurent, L. C. & Garrett, C. 2002 The role of internal tides in mixing the deep ocean. *J. Phys. Oceanogr.* **32**, 2882–2899.

Tabaei, A., Akylas, T. R. & Lamb, K. G. 2005 Nonlinear effects in reflecting and colliding internal wave beams. *J. Fluid Mech.* **526**, 217–243.

Zhang, H. P., King, B. & Swinney, H. L. 2007 Experimental study of internal gravity waves generated by supercritical topography. *Phys. Fluids* **19**, 096602.